

# Recovering the second moment of the strain distribution from neutron Bragg edge data

K. Fogarty,<sup>1,2</sup> E. Ametova,<sup>3,1</sup> G. Burca,<sup>4,1</sup> A.M. Korsunsky,<sup>5</sup> S. Schmidt,<sup>6</sup> P.J. Withers,<sup>7</sup> and W.R.B. Lionheart<sup>1</sup>

<sup>1</sup>*Department of Mathematics, The University of Manchester, Manchester M13 9PL, United Kingdom*

<sup>2</sup>*Department of Physics and Astronomy, The University of Manchester, Manchester M13 9PL, United Kingdom*

<sup>3</sup>*Laboratory for Application of Synchrotron Radiation, Karlsruhe Institute of Technology, Karlsruhe 76131, Germany*

<sup>4</sup>*ISIS Pulsed Neutron and Muon Source, STFC, UKRI, Rutherford Appleton Laboratory, Didcot OX11 0QX, United Kingdom*

<sup>5</sup>*Department of Engineering Science, University of Oxford, Oxford OX1 3PJ, United Kingdom*

<sup>6</sup>*European Spallation Source, Lund S - 221 00, Sweden*

<sup>7</sup>*Henry Royce Institute, Department of Materials, The University of Manchester, Manchester M13 9PL, United Kingdom*

(\*Electronic mail: bill.lionheart@manchester.ac.uk)

(Dated: 20 January 2022)

Point by point strain scanning is often used to map the residual stress (strain) in engineering materials and components. However the gauge volume and hence spatial resolution is limited by the beam defining apertures and can be anisotropic for very low and high diffraction (scattering) angles. Alternatively, wavelength resolved neutron transmission imaging has a potential to retrieve information tomographically about residual strain induced within materials through measurement in transmission of Bragg edges – crystallographic fingerprints which location and shape depend on microstructure and strain distribution. In such a case the spatial resolution is determined by the detector pixel size which for neutrons can be 10-20 smaller than strain scanning gauge volumes. However, Bragg edge strain tomography requires extraction of the second moment (variance about zero) of the strain distribution resolved in the beam direction which has not yet been demonstrated in practice. In this paper we verify experimentally that the second moment can be reliably measured using a previously well characterised aluminium ring and plug sample. We compare experimental measurements against numerical calculation and further support our conclusions through rigorous uncertainty quantification in the estimated mean and variance of the strain distribution.

Residual stress (and thereby elastic strain) is the stress that remains in a body when no external forces are applied<sup>1</sup>. Because these internal stresses add to those arising from externally applied loads, they can give rise to unexpected behaviours and premature failure. Information about the strain within polycrystalline materials is therefore critical importance for understanding the deformation and fracture mechanics of engineered components. Conventionally, diffraction of monochromatic X-rays<sup>2,3</sup> or neutrons<sup>4,5</sup> can be used for non-destructive strain measurements. To achieve high spatial resolution, a sample is raster-scanned with a collimated or focused beam and the angle of the scattered beam  $2\theta$  is recorded to deduce the interplanar spacing, point by point, using Bragg's equation, which is then used to infer strain. This process is repeated for multiple sample orientations and a map of the strain components at every image point (voxel) is recovered. The width of the pencil-beam and consequently of the gauge volume is typically in order of a few millimeters for neutrons<sup>6</sup> and tens of micrometers for X-rays<sup>7</sup>. However, the resolution of this technique is fundamentally limited due to elongation of the gauge volume in the beam direction, particularly at small diffraction angles characteristic of high energy X-ray beams. Other disadvantages include slow acquisition and positional inaccuracies<sup>8</sup>.

By contrast tomographic reconstruction methods can achieve spatial resolutions which are limited by the pixel size used to record the transmission data. Since this can be considerably smaller than the apertures used for strain scanning

there is a significant driver to explore tomographic strain reconstruction methods.

In this respect, a polychromatic neutron beam in a combination with a Time-of-Flight (ToF) area detector can be employed to register both spatial and ToF (wavelength) information about the transmitted neutrons. According to Bragg's law

$$2d_{hkl} \sin \theta = \lambda_{hkl}, \quad (1)$$

coherent elastic scattering at an angle  $\theta$  can happen only for wavelengths  $\lambda$  shorter than twice the spacing between the lattice planes ( $d_{hkl}$ ). Hence, the transmitted spectrum will exhibit a rapid increase in the transmitted intensity at a wavelength  $\lambda$  slightly longer than twice this distance because intensity can no longer be diffracted out of the transmitted beam by this  $hkl$  family of planes. This sharp change in transmission is called a *Bragg edge* and allows the establishment of a relationship between the transmitted neutron spectral fingerprint and the crystallographic phases in the material. Current neutron sensitive microchannel plates (MCP) detectors can have pixel sizes down to around 0.055 mm and ToF accuracy of  $\approx 1 \mu\text{s}$ <sup>9</sup>. Given a sample rotation, Bragg edge strain tomography has a potential to overcome the aforementioned constraints of conventional diffraction strain scanning.

Bragg edge strain tomography seeks to determine the spatial distribution of strain inside a polycrystalline sample from the change in the neutron transmission spectra near a Bragg edge<sup>8,10–13</sup>. Given theoretical ideal conditions and a uniformly strained material, the Bragg edge can be modelled as

a Heaviside function multiplied by a linear function of wavelength<sup>14</sup>. The result of this uniform strain is to shift the relative position (mean) of the Bragg edge with respect to a sample without strain present. However, the mean is insensitive to variations in strain in the interior of the object and cannot provide sufficient information to resolve the strain distribution along the ray path<sup>12</sup>, prohibiting Bragg edge strain tomography. To overcome this problem, tomographic data can be combined with equilibrium equations of elasticity using a finite element approach to find the strain<sup>13</sup>. Alternatively, Lionheart<sup>14</sup> observed that an experimentally measured Bragg edge is representative of the cumulative strain histogram along a neutron ray within the material. Hence, differentiation of the Bragg edge will theoretically return the histogram of strain. The shape of the histogram is the convolution of the histogram for the unstrained case with the histogram of the relevant component of strain along the beam, and the second moment of the deconvolved histogram is the ray transform of the symmetric second tensor power of the strain. Hence, the well-established longitudinal ray transform<sup>15</sup> can be used to reconstruct strain tensor in every voxel. The proposed theoretical method relies on our ability to measure the second moment of the strain distribution in transmission (projection) data which has not yet been demonstrated in practice.

In this paper, we demonstrate that the second moment, the variance about zero, of strain in the ray direction can be captured experimentally. We present an analysis of two reference samples (Fig. 1, a) manufactured within the Versailles Project on Advanced Materials and Standards (VAMAS)<sup>16</sup>. The first sample is a shrink-fit aluminium alloy assembly of ring and plug (henceforth *strained* sample). The ring and the plug have outer diameters of 50 mm and 25 mm, respectively. The second sample is an unstained plug of the same diameter (henceforth *strain-free* reference). Both samples were manufactured under well controlled conditions, are of weak crystallographic texture and low residual stress prior to assembly. In addition they have been extremely well characterised in a global round-robin study<sup>17</sup>.

In order to compare experimental measurements with theoretical predictions, we briefly recall some details about the expected strain in the strained sample. The axial stress of the plug,  $\sigma_{zz}^p$ , the ring  $\sigma_{zz}^r$ , and the interface pressure,  $P$ , have been determined in a series of other experiments<sup>17</sup> and have been found to be  $-15$  MPa,  $5$  MPa and  $48$  MPa, respectively. The values of Poisson's ratio,  $\nu$ , and the Young's modulus,  $E$ , of the material were taken to be  $0.33$  and  $68$  GPa respectively. The radial and hoop strain can be obtained via solving the governing equations of linear elastic theory<sup>18</sup>. Assuming that the axis of the cylinder is perpendicular to the direction of travel of the sufficiently parallel neutron beam, the strain along the ray path,  $\varepsilon$ , is related to the radial ( $\varepsilon_{rr}$ ) and hoop ( $\varepsilon_{\theta\theta}$ ) components of strain via  $\varepsilon = \varepsilon_{rr} \sin^2 \phi + \varepsilon_{\theta\theta} \cos^2 \phi$ , where  $\phi$  is the angle anticlockwise from the neutron direction of travel. We will refer to the resulting distribution of strain as the *projected strain*. We discretise the analytical strain map onto the experimental detector grid and sample from this array to calculate the first and the second moments of the distribution along the ray path. Fig 1, b-d shows the individual contour maps of the

two calculated components of strain and their sum.

The sample was measured<sup>20</sup> at the Imaging and Materials Science & Engineering (IMAT) beamline operating at the ISIS spallation neutron source (Rutherford Appleton Laboratory, UK)<sup>21,22</sup>. At a pulsed neutron source, wavelength discrimination is achieved by measuring the time between neutron generation and detection (ToF) which is subsequently converted to wavelength using the de Broglie equation. The MCP detector<sup>9,23</sup> was configured to record 2897 wavelength channels between  $3.12$  Å and  $5.12$  Å. To reduce the undesirable effect of counts loss<sup>24</sup>, two shutter intervals were set in ToF (wavelength) domain with resolution  $7.21 \cdot 10^{-4}$  Å and  $3.60 \cdot 10^{-4}$  Å, respectively. The MCP detector has  $512 \times 512$  pixels,  $0.055$  mm pixel size, giving a field of view of approximately  $28 \times 28$  mm<sup>2</sup>. A visible laser beam was used to align the vertical axis of the sample with respect to the vertical edge of the detector and to ensure that the plug, the ring and their interface are in the field-of-view (Fig. 2, a). Subsequently, the strain-free reference sample was aligned and centered vertically and measured.

Individual projections of samples and a single normalisation image were measured with 4 hours long exposure. Flat-field and MCP detector related corrections<sup>24</sup> were adapted from BEAn<sup>25</sup> and applied to the projections. As the strained sample is axially symmetric, of weak crystallographic texture and only a radial-hoop internal stress, we assume that the strain does not vary vertically. Consequently, we sum over each vertical column of pixels to improve the signal-to-noise ratio. Such aggregated pixels are commonly referred to as *macro-pixels*.

Given the measured wavelength range, two distinct Bragg edges were present in the acquired spectra,  $\lambda \approx 4.0$  Å and  $\lambda \approx 4.7$  Å, with the latter one more pronounced and also sampled with higher wavelength resolution (Fig. 2, b). Therefore we performed analysis only for the latter edge. To model the transmission spectra around the Bragg edge we used the Santisteban function<sup>26</sup>

$$\text{Tr}(\Lambda, \psi) = \exp(-(a_0 + b_0\Lambda))(1 - \exp(-(a_1 + b_1\Lambda)))B(\Lambda) \quad (2)$$

where  $\Lambda$  is the experimentally acquired transmission signal measured in Å and  $\psi = (a_0, b_0, a_1, b_1)$  is a vector of the model parameters.

Here,  $a_0, b_0$  and  $a_1, b_1$  describe the exponential attenuation to the right (tail) and to the left (pedestal) of the Bragg-edge, respectively, and  $B(\Lambda)$  is given by

$$B(\Lambda) = \frac{1}{2} \left[ \text{erfc} \left( -\frac{\Lambda - \lambda_{hkl}}{\sqrt{2}\sigma} \right) - \exp \left( -\frac{\Lambda - \lambda_{hkl}}{\tau} + \frac{\sigma^2}{2\tau^2} \right) \times \text{erfc} \left( -\frac{\Lambda - \lambda_{hkl}}{\sqrt{2}\sigma} + \frac{\sigma}{\tau} \right) \right].$$

where  $\lambda_{hkl}$  is the position of the Bragg-edge,  $\tau$  is the moderator decay constant, and  $\sigma$  is the Gaussian broadening due to the sample and instrument. See the supplementary material for derivation of the model.

The model<sup>26</sup> was not explicitly derived to account for strain but rather to model blur in the wavelength dimension due to

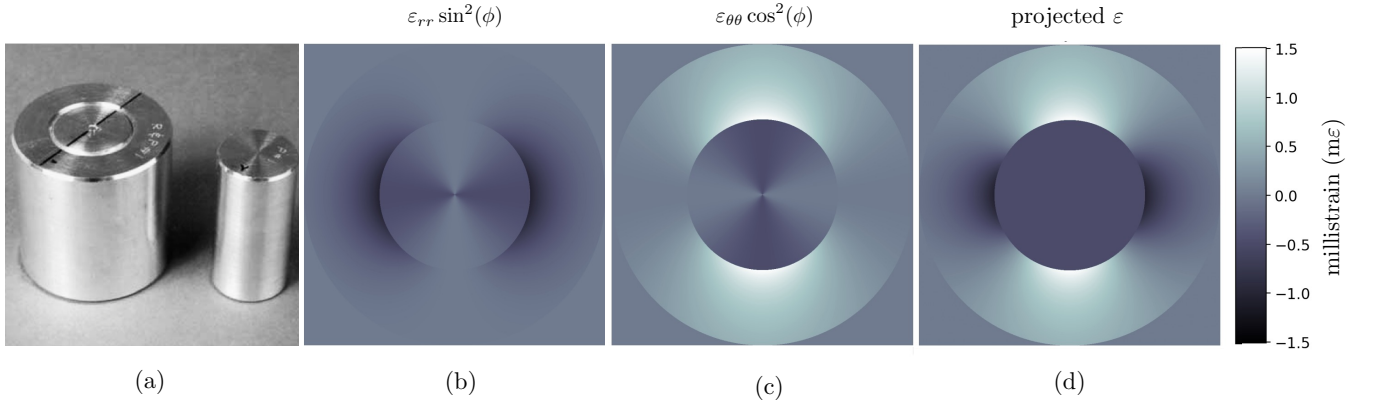


FIG. 1. a) VAMAS round robin shrink fitted aluminium ring-and-plug and plug test samples (figure taken from the VAMAS report<sup>19</sup>). b)  $\epsilon_{\theta\theta}$  component of the strain tensor scaled by  $\cos^2\phi$ . c)  $\epsilon_{rr}$  component of the strain tensor scaled by  $\sin^2\phi$ . d) Plot of the expected strain ( $\epsilon = \epsilon_{\theta\theta} \cos^2\phi + \epsilon_{rr} \sin^2\phi$ ) within the strained sample for a ray path from top to bottom of the figure ( $\phi = 0$ ).

the stochastic nature of neutron production and the geometric effects of the beamline<sup>27,28</sup>. Nevertheless the sensitivity of the model to strain was demonstrated in several studies<sup>29–32</sup>.

We used the non-linear least square fitting (Levenberg–Marquardt algorithm) to fit the model function (eq. 2) and estimate parameters. To avoid the local minimum problem common to the non-linear fitting, we employ a three stage fitting process<sup>26</sup>. An example of a measured Bragg edge overlaid with the fitted model function is shown in Fig. 2, c.

The *first moment* (mean) of the projected strain is given by<sup>33</sup>:

$$\langle \epsilon \rangle = \frac{\lambda_{hkl}^s - \lambda_{hkl}^f}{\lambda_{hkl}^f} \quad (3)$$

where  $\lambda_{hkl}^f$  and  $\lambda_{hkl}^s$  are the position of Bragg edge for the strain-free sample and the strained samples, respectively.

Our strategy for the measurement of the *second moment* (variance about zero) is as follows. The value of  $\tau$  is a function of the geometry and temperature of the moderator used in the experiment<sup>25</sup>; as these parameters remained approximately constant within the experiment,  $\tau$  is expected to be constant. Parameter  $\sigma$  is a function of width of the initial pulse from the moderator and sample-related broadening<sup>34</sup>. As the shape of the pulse is expected to be repeatable and uniform in the spatial dimension, any spatial change in  $\sigma$  can be attributed to the change in variance of strain in the beam direction. Although  $\sigma$  in eq. 2 captures broadening of the Bragg edge, we need to establish a relationship between an instrument response and the variance of strain along a beam direction. Assuming a linear relationship, the model of measurements is given by  $y = mx + c$ , where  $x = [x_0, x_1, \dots, x_{j-1}]$  is a vector of the theoretically predicted variance of strain in the beam direction at detector macro-pixel  $j$  between 0 and 511 and  $y = [\sigma_0, \sigma_1, \dots, \sigma_{j-1}]$  is experimentally measured  $\sigma$  at each macro-pixel  $j$ . We use linear regression to define parameters  $m$  and  $c$ . Obviously, this simple proof-of-concept measurement model cannot substitute a proper instrument scale calibration necessary to establish this tomographic measure-

ment technique.

To support our findings, we perform uncertainty quantification based on Bayesian interference<sup>35</sup>. In the Bayesian framework, the measurement model is represented as a joint probability distribution of unknown parameters  $\eta$  and observations  $\mathbf{Y}$

$$\pi(\eta|\mathbf{Y}) = \frac{\pi(\mathbf{Y}|\eta)\pi(\eta)}{\pi(\mathbf{Y})}, \quad (4)$$

where  $\pi(\mathbf{Y}|\eta)$  is the *likelihood* function of  $\eta$ , i.e., the predictive distribution of  $\mathbf{Y}$ , given  $\eta$ . The *prior* distribution  $\pi(\eta)$  encodes the prior knowledge and model assumptions. The *model evidence*  $\pi(\mathbf{Y})$  maps the likelihood, prior and observations to a single value that describes the probability of observation. Finally,  $\pi(\eta|\mathbf{Y})$  is the *posterior* probability: the probability of  $\eta$  after  $\mathbf{Y}$  is observed.

The mean of the likelihood is given by the parametric model for each data point. Let  $j$  between 0 and 511 denote the position of a column of pixels and  $[\mathbf{Y}_j]_i = \mathbf{Y}(\lambda_i)_j$  be the mean measured transmission for wavelength bin  $i$  in pixel column  $j$ . We model the transmission error over a macro-pixel as additive Gaussian noise with zero mean and a variance that is linearly dependent on the transmission<sup>33</sup>. Then,

$$\mathbf{Y}(\lambda_i)_j = \text{Tr}(\lambda_i|\psi_j) + \xi(\omega|\lambda_i, j), \quad (5)$$

where  $\xi(\omega|\lambda_i, j)$  is a Gaussian random variable

$$\xi(\omega|\lambda_i, j) \sim \mathcal{N}(0, s(\lambda_i)_j^2), \quad (6)$$

and  $s(\lambda_i)_j^2$  is the unbiased estimate of the sample variance. Then, the likelihood  $\pi(\mathbf{Y}|\eta)$  is given by

$$\pi(\mathbf{Y}(\lambda_i)_j|\psi_j) = \pi(\xi(\omega|\lambda_i, j) = \mathbf{Y}(\lambda_i)_j - \text{Tr}(\lambda_i|\psi_j)) \quad (7)$$

$$\propto \exp\left(-\frac{1}{2} \|\mathbf{Y}(\lambda_i)_j - \text{Tr}(\lambda_i|\psi_j)\|_{\Sigma}^2\right), \quad (8)$$

where  $\|\cdot\|_{\Sigma}^2$  is the covariance-weighted norm. Finally, we

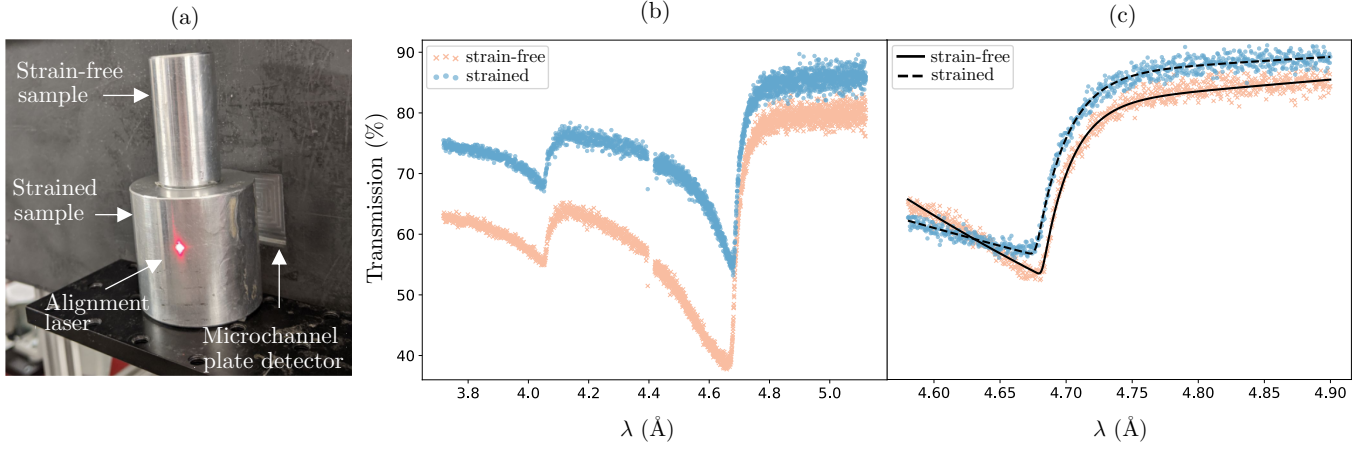


FIG. 2. a) Scheme illustrating experimental data acquisition. b) Plot showing the transmission of neutrons (%) in a single macro-pixel as a function of wavelength. A gap in the recorded spectra is caused by detector dead time. c) Measured Bragg edge in a single macro-pixel overlaid with the fitted model function.

converge to

$$\pi(Y(\lambda_i)_j | \psi_j) = \exp \left( - \sum_{\lambda_i} \frac{1}{2s(\lambda_i)} \left( Y(\lambda_i) - \text{Tr}(\lambda_i | \psi_j) \right)^2 \right). \quad (9)$$

The prior distributions on the parameters of the model  $\psi_j$  are assumed to be weakly informative (wide peak) Gaussian's centered at the best estimates obtained from the Levenberg-Marquardt fit for each parameter. We further use the Hamiltonian Monte Carlo (HMC)<sup>36</sup> method to sample from the posterior distribution. Bayesian inference and HMC are implemented using the Python wrapper PySTAN for the probabilistic programming framework STAN.

Fig. 3 compares a maximum a posteriori probability (MAP) estimation of the mean and second moment obtained from the experimental data. Overlaid we plot a confidence interval of two standard deviations of the distribution. For the strain-free case, parameter  $\sigma$  is expected to be constant but greater than 0 as  $\sigma$  also models blur in the wavelength dimension. Therefore the theoretical predictions are given by the best linear fit to estimated data. Theoretical predictions for the strained sample are given by our calculations in fig. 1, d which were scaled linearly to best match data. It can clearly be seen that both mean and variance are within the uncertainty interval for both samples and the main trends are captured. However there is strong noise present in all estimated parameters and for some data points MAP estimate of the second moment is 0 and the 95% confidence interval includes negative values. There are several reasons for the observed behaviours.

Following Hendriks et al.<sup>33</sup>, we assumed Gaussian noise in the measured transmission data. In fig. 4 we show the distribution of error in some representative macro-pixels overlaid with the fitted Gaussian probability density function. While the distributions have a clear bell-shape, they are also skewed towards negative values. Conducting a combined D'Agostino and Pearson's omnibus test<sup>37</sup> with a significance level of  $\alpha = 0.001$  showed that of the 741,376 distributions consid-

ered 690,688 have enough evidence to reject the hypothesis that the data was drawn from a Gaussian distribution. The reason for this skew might be the overlap correction<sup>24</sup> used to compensate for counts loss. The correction relies on Poisson statistics and the weighting factor for each wavelength bin is calculated based on values in shorter wavelength bins introducing inter-bin correlations and potentially a skew in the data.

The Santisteban model<sup>26</sup> was not designed to account for strain and the parameter  $\sigma$ , which was used in this study as a measure of strain variance, does not have any physical meaning in the model. Secondly, the model assumes the Gaussian distribution of strain. In fig. 5 we show a posterior distribution of  $\sigma$  for both samples. For the strained sample we chose a data point where the fitting resulted in  $\sigma = 0$ . The posterior distribution is concentrated at  $\sigma = 0$ , consistent with least-square fit. For the strain-free sample, the posterior distribution is multimodal with two pronounced peaks. Both distributions highlight inadequacy of the Santisteban model for uniquely identifying the second moment of the strain distribution. Therefore, more research is needed to have more accurate physical Bragg edge model for strain measurements.

To conclude, we have demonstrated that the second-order moment of the strain distribution can be obtained experimentally. The theoretically predicted first and second moments are covered by the 95% confidence interval estimated through Bayesian inference. However we found out that Gaussian nature of the transmission error could only be established with relatively low confidence. Further work in this area should seek to improve our confidence in the choice of likelihood. Furthermore, the posterior distribution shows direct evidence that the semi-empirical Santisteban model is inadequate for uniquely extracting higher order moments in general. Therefore a model that explicitly accounts for the moments of the strain distribution and for texture effects in the material is needed. Despite the limitations of the current study, our findings pave the way for neutron strain tomography. The task of

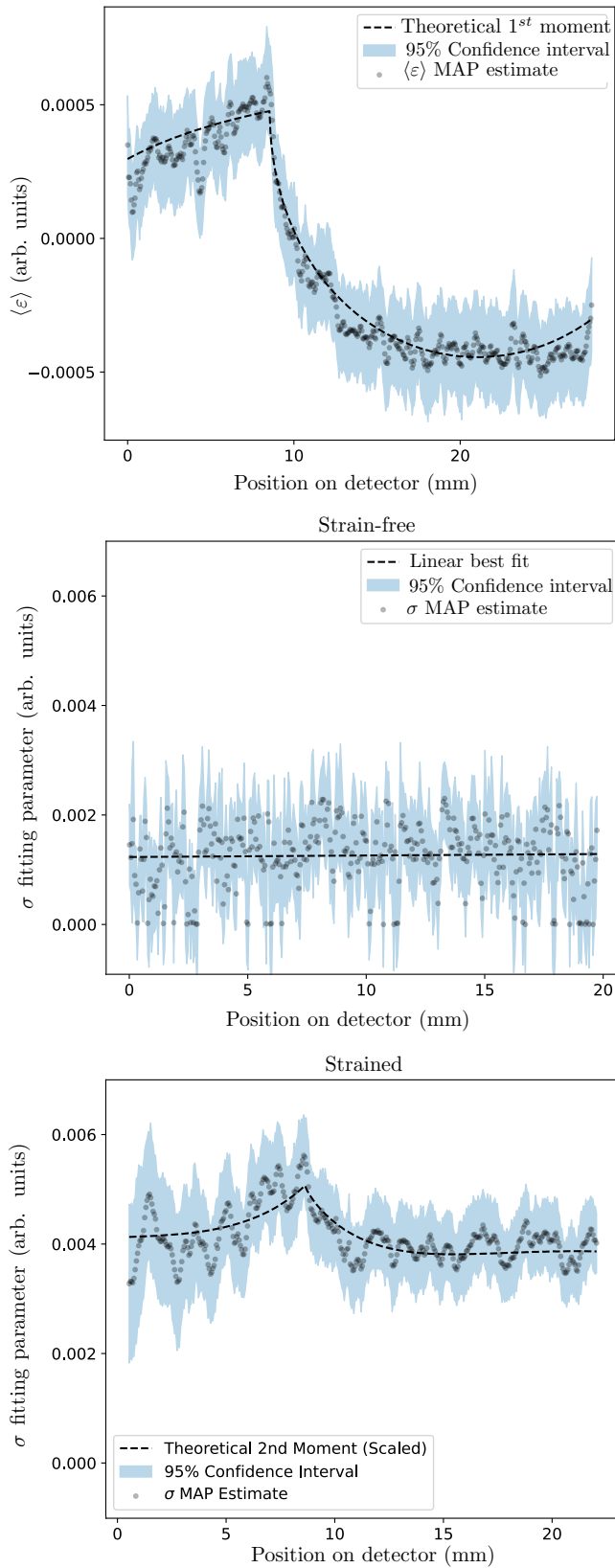


FIG. 3. Variation in the second moments as a function of detector pixel obtained via HMC Bayesian inference. MAP estimate refers to the position of the maximum posterior density and the 95% is found from  $\pm 2$  standard deviations of the posterior distribution.

more accurate Bragg edge modeling, calibration and uncertainty quantification is an opportunity for future research.

See the supplementary material for derivation of the Santisteban model.

## ACKNOWLEDGMENT

Authors would like to thank Dr S. Cotter, and Dr J. Hendriks for their input and ideas at various stages in this project.

## DATA AVAILABILITY STATEMENT

The data that support the findings of this study will be openly available following an embargo at the following URL/DOI: 10.5286/ISIS.E.RB1920056<sup>20</sup>. Data will be available from 27 November 2022. Until the embargo period expires, data are available from the corresponding author upon reasonable request.

## FUNDING

This work was funded by EPSRC grants “A Reconstruction Toolkit for Multichannel CT” (EP/P02226X/1) and “Rich Nonlinear Tomography for advanced materials” (EP/V007742/1). We gratefully acknowledge beamtime RB1920056 (URL/DOI: 10.5286/ISIS.E.RB1920056)<sup>20</sup> at the IMAT Beamline of the ISIS Neutron and Muon Source, Harwell, UK. K F acknowledges the support of the EPSRC grant “EPSRC Centre for Doctoral Training in Agri-Food Robotics” (EP/S023917/1) in the final stages of this work. E A was partially funded by the Federal Ministry of Education and Research (BMBF) and the Baden-Württemberg Ministry of Science as part of the Excellence Strategy of the German Federal and State Governments. W R B L acknowledges support from a Royal Society Wolfson Research Merit Award.

## REFERENCES

- <sup>1</sup>P. J. Withers and H. Bhadeshia, “Residual stress. Part 1—measurement techniques,” *Materials science and Technology* **17**, 355–365 (2001), DOI: <https://doi.org/10.1179/026708301101509980>.
- <sup>2</sup>H. Poulsen, S. Garbe, T. Lorentzen, D. Juul Jensen, F. Poulsen, N. Andersen, T. Frello, R. Feidenhans'l, and H. Graafsma, “Applications of high-energy synchrotron radiation for structural studies of polycrystalline materials,” *Journal of synchrotron radiation* **4**, 147–154 (1997), DOI: <https://doi.org/10.1107/S0909049597002021>.
- <sup>3</sup>W. Kabsch, “Evaluation of single-crystal X-ray diffraction data from a position-sensitive detector,” *Journal of Applied Crystallography* **21**, 916–924 (1988), DOI: <https://doi.org/10.1107/S0021889888007903>.
- <sup>4</sup>A. Frischbutter, D. Neov, C. Scheffzük, M. Vrana, and K. Walther, “Lattice strain measurements on sandstones under load using neutron diffraction,” *Journal of Structural Geology* **22**, 1587–1600 (2000), DOI: [https://doi.org/10.1016/S0191-8141\(00\)00110-3](https://doi.org/10.1016/S0191-8141(00)00110-3).
- <sup>5</sup>M. R. Daymond and N. W. Bonner, “Measurement of strain in a titanium linear friction weld by neutron diffraction,” *Physica B: Condensed Matter* **325**, 130–137 (2003), DOI: [https://doi.org/10.1016/S0921-4526\(02\)01514-4](https://doi.org/10.1016/S0921-4526(02)01514-4).



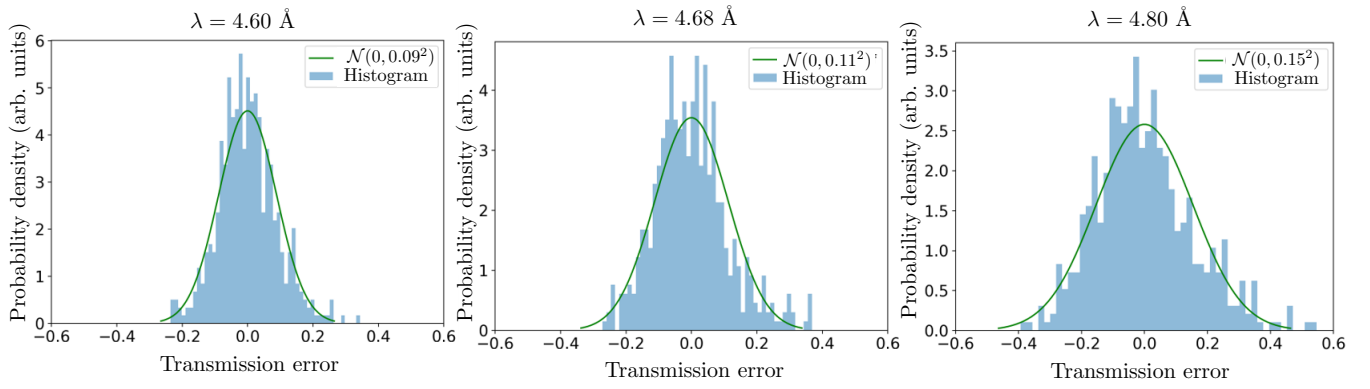


FIG. 4. Histograms showing the distribution of the error for different values of transmission for the central column of the detector pixels. A Gaussian probability density function has been fitted to the data (solid line).

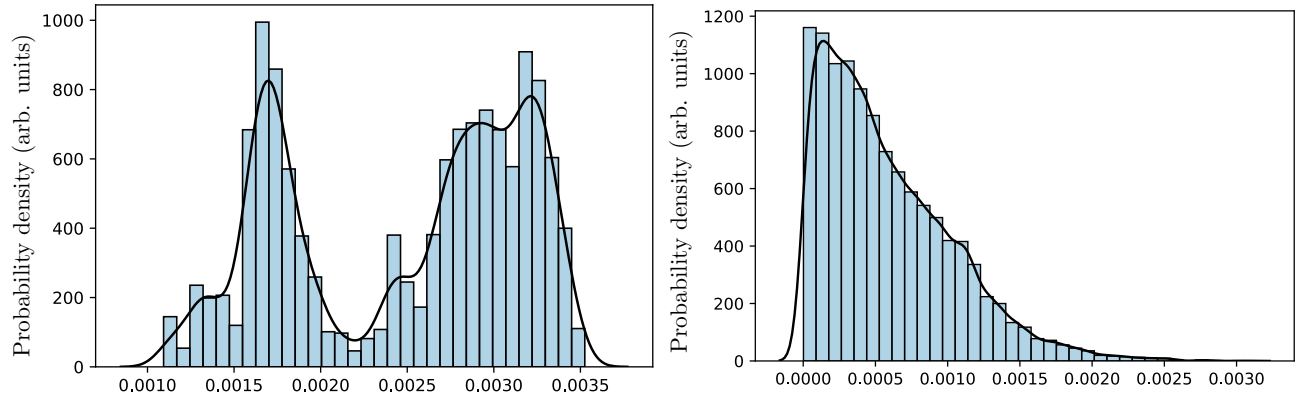


FIG. 5. Histograms of the posterior density of the  $\sigma$  parameter for detector column 110 of the strain-free sample (left) and for detector column 90 of the strained sample (right) shown; the solid line shows the kernel density estimate plot for the same distribution.

- <sup>6</sup>P. Withers, M. Johnson, and J. Wright, “Neutron strain scanning using a radially collimated diffracted beam,” *Physica B: Condensed Matter* **292**, 273–285 (2000), DOI: [https://doi.org/10.1016/S0921-4526\(00\)00481-6](https://doi.org/10.1016/S0921-4526(00)00481-6).
- <sup>7</sup>A. M. Korsunsky, K. E. Wells, and P. J. Withers, “Mapping two-dimensional state of strain using synchrotron X-ray diffraction,” *Scripta Materialia* **39**, 1705–1712 (1998), DOI: [https://doi.org/10.1016/S1359-6462\(98\)00385-6](https://doi.org/10.1016/S1359-6462(98)00385-6).
- <sup>8</sup>B. Abbey, S. Y. Zhang, M. Xie, X. Song, and A. M. Korsunsky, “Neutron strain tomography using Bragg-edge transmission,” *International journal of materials research* **103**, 234–241 (2012), DOI: <https://doi.org/10.3139/146.110674>.
- <sup>9</sup>A. S. Tremsin, J. V. Vallerger, J. B. McPhate, O. H. Siegmund, and R. Raffanti, “High resolution photon counting with MCP-Timex quad parallel readout operating at >1 KHz frame rates,” *IEEE transactions on nuclear science* **60**, 578–585 (2012), DOI: <https://doi.org/10.1109/TNS.2012.2223714>.
- <sup>10</sup>B. Abbey, S. Y. Zhang, W. J. Vorster, and A. M. Korsunsky, “Feasibility study of neutron strain tomography,” *Procedia Engineering* **1**, 185–188 (2009), DOI: <https://doi.org/10.1016/j.proeng.2009.06.043>.
- <sup>11</sup>B. Abbey, S. Y. Zhang, W. Vorster, and A. M. Korsunsky, “Reconstruction of axisymmetric strain distributions via neutron strain tomography,” *Nuclear Instruments and Methods in Physics Research Section B: Beam Interactions with Materials and Atoms* **270**, 28–35 (2012), DOI: <https://doi.org/10.1016/j.nimb.2011.09.012>.
- <sup>12</sup>W. R. Lionheart and P. J. Withers, “Diffraction tomography of strain,” *Inverse Problems* **31**, 045005 (2015), DOI: <https://doi.org/10.1088/0266-5611/31/4/045005>.
- <sup>13</sup>A. Gregg, J. Hendriks, C. Wensrich, *et al.*, “Bragg-edge neutron strain tomography: A review and path forward to general tomographic reconstruction,” in *9th Australasian Congress on Applied Mechanics (ACAM9)* (Engineers Australia Sydney, 2017) pp. 274–282.
- <sup>14</sup>W. R. Lionheart, “Histogram tomography,” *Mathematics in Engineering* **2**, 55–74 (2020), DOI: <https://doi.org/10.3934/mine.2020004>.
- <sup>15</sup>V. A. Sharafutdinov, *Integral geometry of tensor fields*, Vol. 1 (Walter de Gruyter, 2012).
- <sup>16</sup>G. Webster and R. Wimpory, “Polycrystalline materials. Determinations of residual stresses by neutron diffraction,” *ISO/TTA3 Technology Trends Assessment*, Geneva **20** (2001).
- <sup>17</sup>M. Daymond, M. Johnson, and D. Sivia, “Analysis of neutron diffraction strain measurement data from a round robin sample,” *The Journal of Strain Analysis for Engineering Design* **37**, 73–85 (2002), DOI: <https://doi.org/10.1243/0309324021514844>.
- <sup>18</sup>M. Boin, *Developments towards the tomographic imaging of local crystallographic structures*, Ph.D. thesis, The Open University, Milton Keynes (2011).
- <sup>19</sup>G. A. Webster, *Neutron diffraction measurements of residual stress in a shrink-fit ring and plug* (National Physical Laboratory, 2000).
- <sup>20</sup>W. R. B. Lionheart, G. Burca, A. Korsunsky, M. Turner, J. S. Jørgensen, S. Schmidt, J. Kelleher, K. Yan, P. J. Withers, and E. Ametova, “Can the second moment of the Bragg edge be resolved for neutron strain measurement?” *STFC ISIS Neutron and MuonSource* (2019), DOI: <https://doi.org/10.5286/ISIS.E.100529645>.

- <sup>21</sup>G. Burca, W. Kockelmann, J. James, and M. E. Fitzpatrick, “Modelling of an imaging beamline at the ISIS pulsed neutron source,” *Journal of Instrumentation* **8**, P10001 (2013), DOI: <https://doi.org/10.1088/1748-0221/8/10/P10001>.
- <sup>22</sup>W. Kockelmann, T. Minniti, D. E. Pooley, G. Burca, R. Ramadhan, F. A. Akeroyd, G. D. Howells, C. Moreton-Smith, D. P. Keymer, J. Kelleher, *et al.*, “Time-of-flight neutron imaging on IMAT@ ISIS: a new user facility for materials science,” *Journal of Imaging* **4**, 47 (2018), DOI: <https://doi.org/10.3390/jimaging4030047>.
- <sup>23</sup>A. Tremsin, J. McPhate, W. Kockelmann, J. Vallerger, O. Siegmund, and W. Feller, “High resolution Bragg edge transmission spectroscopy at pulsed neutron sources: proof of principle experiments with a neutron counting MCP detector,” *Nuclear Instruments and Methods in Physics Research Section A: Accelerators, Spectrometers, Detectors and Associated Equipment* **633**, S235–S238 (2011), DOI: <https://doi.org/10.1016/j.nima.2010.06.176>.
- <sup>24</sup>A. Tremsin, J. Vallerger, J. McPhate, and O. Siegmund, “Optimization of Timepix count rate capabilities for the applications with a periodic input signal,” *Journal of Instrumentation* **9**, C05026 (2014), DOI: <https://doi.org/10.1088/1748-0221/9/05/C05026>.
- <sup>25</sup>A. Liptak, G. Burca, J. Kelleher, E. Ovtchinnikov, J. Maresca, and A. Horner, “Developments towards Bragg edge imaging on the IMAT beamline at the ISIS pulsed neutron and muon source: BEAn software,” *Journal of Physics Communications* **3**, 113002 (2019), DOI: <https://doi.org/10.1088/2399-6528/ab5575>.
- <sup>26</sup>J. Santisteban, L. Edwards, A. Steuwer, and P. Withers, “Time-of-flight neutron transmission diffraction,” *Journal of Applied Crystallography* **34**, 289–297 (2001), DOI: <https://doi.org/10.1107/S0021889801003260>.
- <sup>27</sup>P. Suortti, M. Ahtee, and L. Unonius, “Voigt function fit of X-ray and neutron powder diffraction profiles,” *Journal of Applied Crystallography* **12**, 365–369 (1979), DOI: <https://doi.org/10.1107/S002188987901270X>.
- <sup>28</sup>F. Kropff, J. Granada, and R. Mayer, “The Bragg lineshapes in time-of-flight neutron powder spectroscopy,” *Nuclear Instruments and Methods in Physics Research* **198**, 515–521 (1982), DOI: [https://doi.org/10.1016/0167-5087\(82\)90293-9](https://doi.org/10.1016/0167-5087(82)90293-9).
- <sup>29</sup>J. R. Santisteban, L. Edwards, M. E. Fitzpatrick, A. Steuwer, P. J. Withers, M. R. Daymond, M. W. Johnson, N. Rhodes, and E. M. Schoon-evel, “Strain imaging by Bragg edge neutron transmission,” *Nuclear Instruments and Methods in Physics Research Section A: Accelerators, Spectrometers, Detectors and Associated Equipment* **481**, 765–768 (2002), DOI: [https://doi.org/10.1016/S0168-9002\(01\)01256-6](https://doi.org/10.1016/S0168-9002(01)01256-6).
- <sup>30</sup>R. Woracek, D. Penumadu, N. Kardjilov, A. Hilger, M. Strobl, R. Wimpory, I. Manke, and J. Banhart, “Neutron Bragg-edge-imaging for strain mapping under in situ tensile loading,” *Journal of Applied Physics* **109**, 093506 (2011), DOI: <https://doi.org/10.1063/1.3582138>.
- <sup>31</sup>A. Tremsin, J. McPhate, A. Steuwer, W. Kockelmann, A. M Paradowska, J. Kelleher, J. Vallerger, O. Siegmund, and W. Feller, “High-resolution strain mapping through time-of-flight neutron transmission diffraction with a microchannel plate neutron counting detector,” *Strain* **48**, 296–305 (2012), DOI: <https://doi.org/10.1111/j.1475-1305.2011.00823.x>.
- <sup>32</sup>A. S. Tremsin, J. B. McPhate, J. V. Vallerger, O. H. Siegmund, W. Kockelmann, A. Paradowska, S. Y. Zhang, J. Kelleher, A. Steuwer, and W. B. Feller, “High-resolution strain mapping through time-of-flight neutron transmission diffraction,” in *Materials Science Forum*, Vol. 772 (Trans Tech Publ, 2014) pp. 9–13, DOI: <https://doi.org/10.4028/www.scientific.net/MSF.772.9>.
- <sup>33</sup>J. Hendriks, N. O’Dell, A. Wills, A. Tremsin, C. Wensrich, and T. Shinohara, “Bayesian non-parametric Bragg-edge fitting for neutron transmission strain imaging,” *The Journal of Strain Analysis for Engineering Design*, 0309324720959237 (2020), DOI: <https://doi.org/10.1177/0309324720959237>.
- <sup>34</sup>R. S. Ramadhan, W. Kockelmann, T. Minniti, B. Chen, D. Parfitt, M. E. Fitzpatrick, and A. S. Tremsin, “Characterization and application of Bragg-edge transmission imaging for strain measurement and crystallographic analysis on the IMAT beamline,” *Journal of Applied Crystallography* **52**, 351–368 (2019), DOI: <https://doi.org/10.1107/S1600576719001730>.
- <sup>35</sup>E. T. Jaynes, *Probability theory: The logic of science* (Cambridge university press, 2003).
- <sup>36</sup>M. Betancourt, “A conceptual introduction to Hamiltonian Monte carlo,” arXiv preprint [arXiv:1701.02434](https://arxiv.org/abs/1701.02434) (2017).
- <sup>37</sup>R. B. d’Agostino, “An omnibus test of normality for moderate and large size samples,” *Biometrika* **58**, 341–348 (1971), DOI: <https://doi.org/10.1093/biomet/58.2.341>.